Study on contrast variations with depth in focused plenoptic cameras

Charlotte Herzog, Xavier Granier, Fabrice Harms, Philippe Zeitoun, Ombeline de La Rochefoucauld

Study on Contrast Variations with Depth in Focused Plenoptic Cameras

CHARLOTTE HERZOG[1,2,3], XAVIER GRANIER[2,4], FABRICE HARMS[1], PHILIPPE ZEITOUN[5], AND OMBELINE DE LA ROCHEFOUCAULD[1,*]

[1] Imagine Optic, Rue François Mitterand, F-33400 Talence, France
[2] Université de Bordeaux, Laboratoire Photonique, Numérique et Nanosciences, UMR 5298, Rue François Mitterrand, F-33400 Talence, France
[3] Inria Bordeaux Sud-Ouest, 200 avenue de la Vieille Tour, F-33405 Talence cedex, France
[4] UMS Archéovision 3D SHS, Université Bordeaux Montaigne, Archéopôle d'Aquitaine, Esplanade des Antilles, F-33607 Pessac cedex, France
[5] Laboratoire d'Optique Appliquée – ENSTA-ParisTech, 828 bvd des Marechaux, F-91762 Palaiseau cedex, France
[*] Corresponding author: odlrochefoucauld@imagine-optic.com

Compiled September 30, 2019

A focused plenoptic camera has the ability to record and separate spatial and directional information of the incoming light. Combined with the appropriate algorithm, 3D scene could be reconstructed from a single acquisition, over a depth range called plenoptic Depth-of-Field. In this article, we study the contrast variations with depth as a way to assess plenoptic Depth-of-Field. We take into account the impact of diffraction, defocus and, magnification on the resulting contrast. We measure the contrast directly on both simulated and acquired images. We demonstrate the importance of diffraction and magnification in the final contrast. Contrary to classical optics, the maximum of contrast is not centered around the main object plane, but around a shifted position, with a fast and non-symmetric decrease of contrast.

https://doi.org/10.1364/OL.44.004825

1. INTRODUCTION

Light-Field imaging is a technology that samples a part of the Light-Field (LF) defined as the radiance flowing through each point and direction of a scene [1–3]. It allows to retrieve more information than in conventional imaging, by separating angular and spatial information contained in the incoming light. It enables new applications such as synthetic aperture, viewpoint changes, depth estimation and 3D imaging [4, 5]. Plenoptic Cameras are Light-Field imaging systems composed of a main lens (ML), a microlens array (MLA) and, a detector [6].

The main advantage of a plenoptic system is the possibility from a single acquisition to reconstruct all the planes of a scene along a depth range that we call plenoptic Depth-of-Field (DoF_{pleno}), defined in [7–10]. Levoy showed theoretical and experimental results in the case of his unfocused light-field microscope [7]. A detailed derivation of DoF_{pleno} equation was presented in [9] but not experimentally validated. Zhu derived a similar equation and confronted it to experimental measurements of a point source [10]. Our work aims at confronting the theoretical DoF_{pleno} to simulations and experiments when imaging with a focused plenoptic camera. We decided to use the contrast as a parameter for assessing if a plane belongs to DoF_{pleno}, as in-focus depth planes are expected to be of higher contrast than out-of-focus ones [5, 11]. Previously reported results either provided a study of the variation of modulation transfer function with depth in the case of an unfocused plenoptic microscope [12], or a characterization of contrast for a focused plenoptic system but without considering its variation with depth [13]. Liang and Ramamoorthi presented a study of contrast along depth but do not consider the effects of diffraction [14].

In this article, we study the variations of contrast with the object's depth for a focused plenoptic system [15, 16]. First, we simulate the expected raw plenoptic sub-images to observe the effects of diffraction, defocus and magnification, separately or combined. Simulated sub-images are then used to determine the variations of contrast with depth. We then confront our simulation results with experimental data.

2. PLENOPTIC DEPTH OF FIELD OF A FOCUSED PLENOPTIC CAMERA

The system studied in this article is a focused plenoptic camera (Fig. 1). The MLA acts as a relay imaging system, re-imaging the image plane of the ML directly on the detector. There is an intrinsic privileged position, that we call reference plane, corresponding to the only plane that is perfectly in focus on the detector. From the physical position of the detector b^{ref}, we calculate the position of the intermediate image plane from the MLA (a^{ref}) and from the ML (z_1^{ref}), and the position of the reference object plane z_0^{ref}. The distances z_1, a and b correspond to the associated distances when choosing an arbitrary z_0. When $a = 0$, the object plane is at a position z_0^{trad}, optically conjugated with the plane positioned at $z_1^{\text{ref}} + a^{\text{ref}}$ from the ML, which corresponds to the physical position of the MLA. This is the traditional (or unfocused) plenoptic configuration [17].

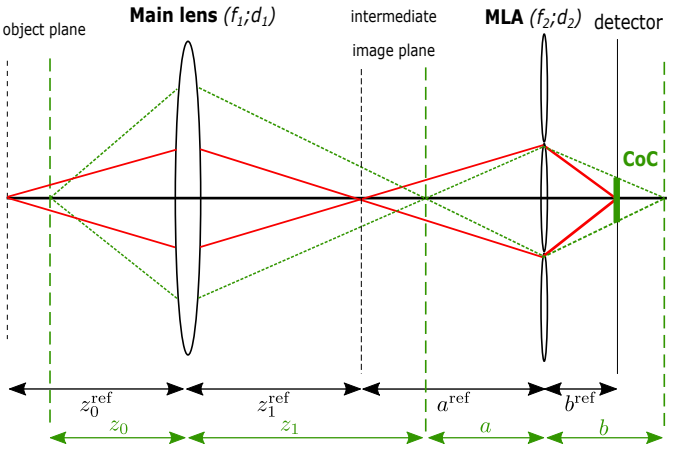

Fig. 1. A focused plenoptic system. Red rays come from the reference depth plane z_0^{ref} whereas green rays correspond to another depth to illustrate the Circle of Confusion (CoC) due to defocus.

We built our own plenoptic setup for visible light in our laboratory. The ML is an achromatic doublet of focal length $f_1 = 200$mm and diameter $d_1 = 24$mm. The MLA is composed of 30×30 square microlenses of focal length $f_2 = 18.6$mm and side $d_2 = 0.3$mm. Each microlens creates a sub-image on the detector. The detector has 1280x960 pixels of size 6.45 μm. The distances used for simulations and experiments are: $z_0^{\text{ref}} = 233$mm, $z_1^{\text{ref}} + a^{\text{ref}} = 1597$mm and $b^{\text{ref}} = 20.7$mm. The object is a 1951 USAF Resolution Test Target (Fig. 2).

Some previous definitions of DoF_{pleno} are based on the same principle of geometrical optics: a depth plane is considered focused if the corresponding defocus blur is bellow a chosen acceptable limit [8–10]. We define DoF_{pleno} in the object plane, taking into account both ML and MLA. A first extension to wave optics is to use the effective pixel size $e = \max(p, s_\lambda)$ (maximum between pixel size p and diffraction limit spot size on the sensor s_λ) [7, 9]. For focused plenoptic cameras, we derive the following equation (similar to Eq. (4) in [7]):

$$DoF_{pleno} = \frac{\lambda}{M^2 \cdot NA_{imMLA}^2} + \frac{e}{m^2 \cdot M^2 \cdot NA_{imMLA}} \quad \textbf{(1)}$$

with $m = b^{\text{ref}}/a$, $M = z_1/z_0$ and $NA_{imMLA} = d_2/(2b^{\text{ref}})$. The first term corresponds to a wave optics term and the second, to a corrected geometrical term. We obtain a DoF_{pleno} of 16.3mm for our configuration.

In our paper, we study the DoF_{pleno} using contrast estimation on a single sub-image. The condition of 3D reconstruction at a chosen depth is that the plane at this depth has been imaged by sharp sub-images: a depth belongs to DoF_{pleno} if and only if it is included in the depth of field of a single sub-image [18]. Therefore, DoF_{pleno} is the depth of field of a single sub-image, and can be directly studied on the raw plenoptic image, without the need for reconstruction. We study the effects of diffraction, defocus and magnification introduced by Eq. (1).

3. SIMULATIONS

A raw plenoptic sub-image is simulated on the detector's plane, positioned at a fixed distance b^{ref} from the MLA (Fig. 1). The simulated object, a portion of a test target (Fig. 2) is placed at a variable distance z_0 from the ML. The distance between the ML and the MLA is kept fixed to $z_1^{\text{ref}} + a^{\text{ref}} = 1597$mm. We consider three phenomena affecting contrast of the raw plenoptic sub-image: diffraction, defocus and magnification.

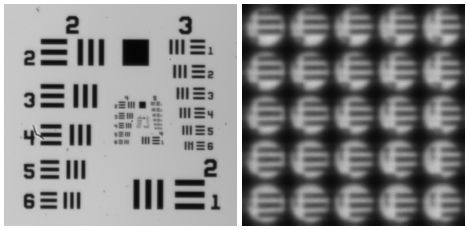

Fig. 2. The 1951 USAF Resolution Test Target used in the experiments (left) and zoom in an experimental raw plenoptic image of group 2.1 (bar width = 125 μm) (right).

Contrast. The contrast used as our criterion is defined by: $(I_{\max} - I_{\min})/(I_{\max} + I_{\min})$, with $I_{\max}$ and $I_{\min}$ the maximal and minimal intensity values measured on the detector plane.

Diffraction. To simulate diffraction, we performed the convolution of the object with a cardinal sine function, representing the diffraction pattern of our square microlenses [19]:

$$\mathrm{I}(r) = I_0 \,\mathrm{sinc}^2\left(\frac{\pi \cdot r \cdot d_2}{\lambda \cdot b^{\text{ref}}}\right) \quad \textbf{(2)}$$

with r the position on the detector, $\mathrm{sinc}(x) = \sin x/x$ and I_0 a normalization constant such that $\int \mathrm{I}(r)\, dr = 1$. Diffraction from ML is ignored, because it is reduced by the mignification of the MLA compared to the sub-image and pixel sizes.

Defocus. The Circle of Confusion corresponds to the region over which a point is blurred in the case of defocus (Fig. 1) [10]. Its diameter CoC is defined as:

$$CoC = d_2 \left|1 - \frac{b^{\text{ref}}}{b}\right| \quad \textbf{(3)}$$

The object is in focus and the image is sharp when the image plane is close to the detector (i.e., $|1 - b^{\text{ref}}/b| << 1$).

Convolutions of the object with I(r) from Eq. (2) and a circle of size CoC from Eq. (3) simulate the effects of diffraction and defocus. They strongly depend on the depth z_0.

Magnification. The third phenomenon is the total magnification M_{tot} of the system, combining the effects of the ML and the MLA. It is a hyperbolic function of depth z_0:

$$M_{\text{tot}} = \frac{z_1}{z_0}\frac{b^{\text{ref}}}{a} = \frac{f_1 b^{\text{ref}}}{z_1^{\text{ref}} + a^{\text{ref}} - f_1}\frac{1}{z_0 - z_0^{\text{trad}}}$$
$$\text{with } z_0^{\text{trad}} = \frac{f_1(z_1^{\text{ref}} + a^{\text{ref}})}{z_1^{\text{ref}} + a^{\text{ref}} - f_1} \quad \textbf{(4)}$$

where z_0^{trad} corresponds to the unfocused plenoptic configuration ($a = 0$).

Impact of diffraction and defocus. Fig. 3 shows the effects of diffraction and defocus on a plenoptic raw sub-image for an object at $z_0 = 240$mm, whereas the optical system is optimized for $z_0^{\text{ref}} = 233$mm. The black dotted curve represents the shape of the original signal without the effects of diffraction or defocus. At $z_0 = 240$mm, the defocus (green curve) only affects the shape and width of the bars, because the size of CoC is too small

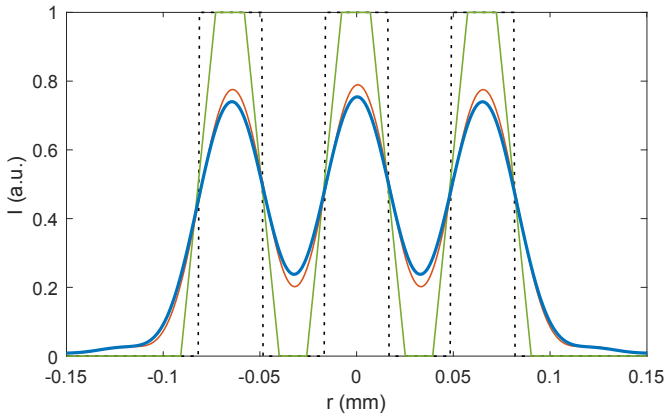

Fig. 3. Simulated 1D raw image of the test object versus position r on the detector with the effect of defocus only (*green*; contrast = 1), with diffraction only (*red*; contrast = 0.59) and with both effects combined (*blue*; contrast = 0.52), calculated at a depth $z_0 = 240$mm, compared to the image with no effect (*dotted black*; contrast = 1).

compared to the width of the bars on the screen to affect the amplitude and contrast of the signal. On the contrary, considering the diffraction (red curve) results in a drop of contrast from 1 to 0.59. With the combination of both diffraction and defocus (blue curve), the contrast is even lower with a value of 0.52.

Impact of diffraction, defocus and magnification. The cumulative effects of the three factors are illustrated in Fig. 4 at four different depths. Magnification governs the spatial frequency of the test object. On the detector, we measure a spatial frequency of 3.20cy/mm, 5.89cy/mm, 8.59cy/mm and 15.34cy/mm for $z_0 =$ 231mm, 233mm, 235mm and 240mm respectively. In comparison, the physical size of the test target of bar width =125μm corresponds to a frequency of 4.00cy/mm.

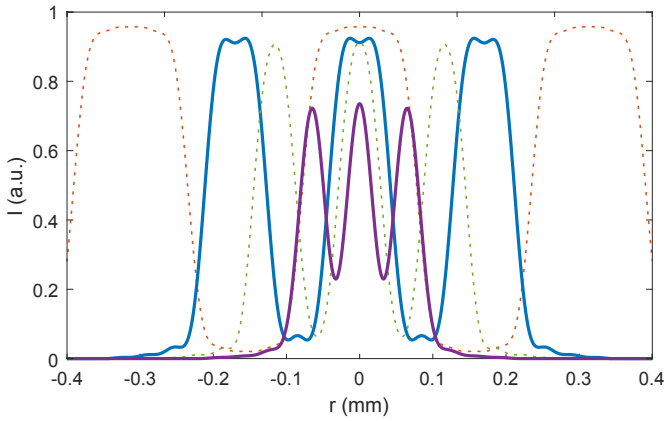

Fig. 4. Simulated 1D raw image with the three effects versus position r on the detector for different depths z_0: $z_0^{\text{ref}} =$ 233mm (*blue*), 231mm (*dotted orange*), 235mm (*dotted green*), and 240mm (*purple*, same depth as in Fig. 3).

The difference in amplitude is mainly due to diffraction and defocus. Magnification plays a role in the amplitude variations, but effects are not symmetric: the contrast is higher close to z_0^{trad} (0.96 at 231mm), and decreases as the depth increases (0.89 at 233mm, 0.86 at 235mm and 0.5 at 240mm). Amplitude at z_0^{ref} is 11% lower in respect to the test target at object plane.

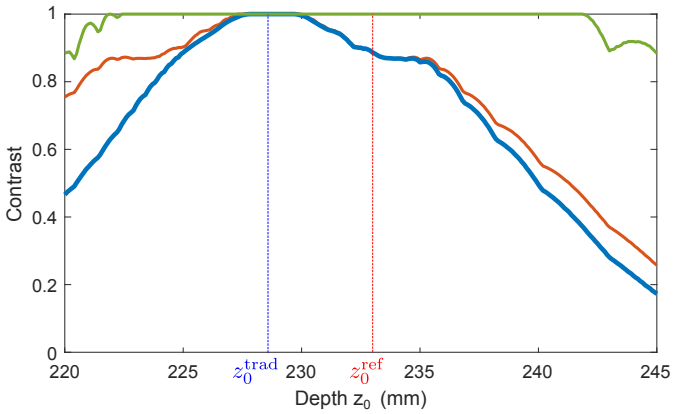

Fig. 5. Contrast curves versus depth: with defocus and magnification only (*green*), with diffraction and magnification only (*orange*) and with the three effects combined (*blue*). Depths $z_0^{\text{ref}} = 233$mm and $z_0^{\text{trad}} = 228.6$mm. Note that the small oscillations are due to pixel discretization of the signal.

Simulated contrast curves. Parameters given in Section 2 were used for the simulations, except that the size of the sub-image has been artificially enlarged to fully include the magnified image. Then the contrast in the simulated raw sub-images was extracted at different depths to study the consequence of the three phenomena (diffraction, defocus and magnification) on the plenoptic image. Fig. 5 shows their impacts on contrast curves as a function of depth position z_0.

In Fig. 5, defocus (green curve) does not significantly affect the contrast as depth varies: a plateau of contrast=1 nearly centered around the z_0^{ref} position is observed, as already seen in Fig. 3. The curve with diffraction and magnification (orange) is maximal at and symmetric around the z_0^{trad} position, and not at the expected z_0^{ref} position. When the three effects are combined (blue curve), the maximum contrast is located around z_0^{trad}. Defocus is responsible for an asymmetry, with a slow decrease of contrast from z_0^{trad} to a plateau around z_0^{ref}. The fast variations in magnification, combined with diffraction and defocus, explain the fast decrease in the contrast curve: higher contrast is measured for larger magnification (around z_0^{trad}), whereas for smaller magnification the image is more affected by defocus and mainly by diffraction. These curves have to be compared to the theoretical value: a region of maximal contrast over 16.3mm around the reference position.

This can be generalized to other sets of parameters: the curves combining magnification with either defocus or diffraction will have similar shapes and will be centered around z_0^{ref} and z_0^{trad} respectively. On the contrary, when the three effects are combined, the shape of the contrast curve will depend on the ratio between magnification, diffraction and defocus.

4. COMPARISON WITH EXPERIMENTAL DATA

Using our setup (cf. Section 2), we imaged a test target at different depths. The optical system was optimized for the reference object plane located at $z_0^{\text{ref}} = 233$mm. Fig. 6a shows sub-images extracted from raw plenoptic images acquired at different depths. In this configuration, total magnification is maximum at the unfocused plenoptic plane $z_0^{\text{trad}} = 228.6$mm, and decreases as depth increases (Eq. (4)). Fig. 6a confirms this effect: at 228.5mm, only a part of one bar appears while as the depth increases, three bars can slowly be seen on the sub-images.

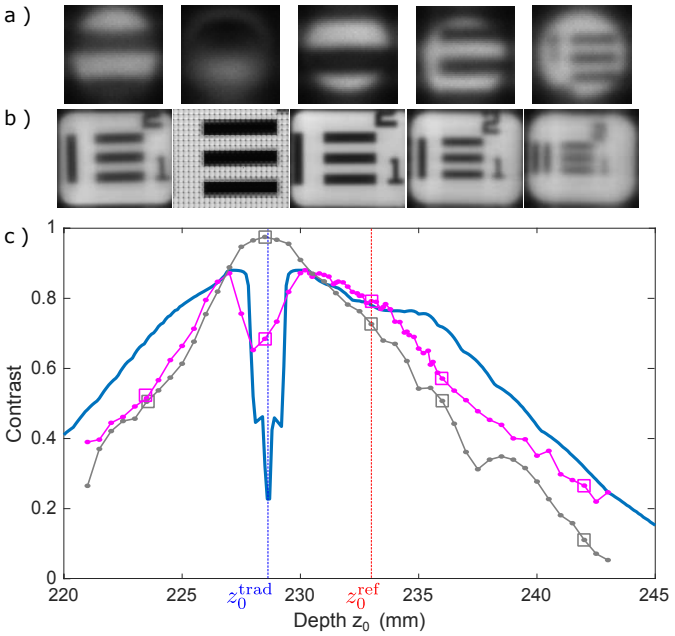

Fig. 6. a) Raw sub-images acquired at planes: $z_0 = 223.5, 228.5, 233, 236, 242$mm; b) Corresponding reconstructed images; c) Comparison of the simulated contrast curve (*blue*) and experimental contrast curve measured on raw sub-images (*pink*) and on reconstructed images (*gray*). The gap located around $z_0^{\text{trad}} = 228.6$mm is due to the large magnification that makes the bars exceeding the sub-image size.

For each experimental raw plenoptic image we measured the contrast of one sub-image taken in the middle of the image, and plot it against depth (pink curve in Fig. 6c). It can be compared to the simulated curve (blue, Fig. 6c), obtained using the parameters of the setup (without the enlarged sub-image size as in Fig. 5).

Both curves present the same shape, with maximal values at $z_0 = 227$ and 230mm surrounding a large gap located at z_0^{trad}. The gap is due to the magnification being so large that the image of the bars does not fit inside the sub-image (as illustrated by the 2^{nd} figure from the left in Fig. 6a). This leads to unreliable contrast values measured on only a part of the total magnified pattern, similarly to what happens in the experimental setup.

On both sides of this gap, the two curves slowly decrease following the decrease in magnification. Near the position z_0^{trad}, magnification is large enough so that diffraction and defocus have little effect on the measured contrast, but when the bars are smaller on the detector, they are more influenced by defocus and mainly by diffraction. At z_0^{ref}, defocus is minimal. Effect of defocus increases when z_0 moves further from z_0^{ref} which explains the asymmetry of the curves around the z_0^{ref} position compared to the left part of the curve.

Although the simulated (blue) and measured (pink) curves are close, they do not overlap. It may be explained by a difference of dynamic ranges: the experimental images are affected by noise and light adjustments that will affect the intensity distribution and thus the measured contrasts in the image.

The quality of a Light-Field imaging depends on the combination of an optical systems with a reconstruction algorithm to compute the final images. In our work, we chose to estimate the contrast on raw sub-images instead of the reconstructed ones. To validate such a choice, we present a contrast curve (in gray, Fig. 6c) computed from images reconstructed at the same depths as in Fig. 6a with the patch tilling method [15] (Fig. 6b) with parameter of refocusing adjusted for each raw image. As expected, the resulting contrast curve (gray) has a similar shape to the one from raw images (pink) except around z_0^{trad}, where it reaches a local maximum instead of a gap.

5. CONCLUSION

In this article, we studied the contrast versus depth in a focused plenoptic camera as an indicator for assessing DoF_{pleno}, the depth range over which a scene can be reconstructed from a single plenoptic raw image. The study of contrast versus depth shows that DoF_{pleno} is more complex than expected by theoretical equations from the literature. We highlighted the combined effects of diffraction, defocus and magnification on the resulting image. Magnification together with diffraction is responsible for important unexpected effects. The contrast curve reaches a maximum at the unfocused plenoptic configuration z_0^{trad} instead of reference depth plane z_0^{ref}. Defocus is responsible for an asymmetry with a slow decrease in-between these two depths and a plateau around z_0^{ref}. Beyond this interval, the contrast decreases quickly due to the fast variations of magnification.

The variations of magnification over the whole depth range is a potential problem for 3D reconstruction: not only is it responsible for contrast reduction, but it will also lead to large variations of size of the imaged sample depending on where it is located. As a solution to this issue, a telecentric plenoptic system can be built, meaning the magnification is constant across depth planes. Furthermore, appropriate algorithms should be used in order to correct for potential size errors.

FUNDING

This work was funded by the VOXEL project (European Union's Horizon 2020 research and innovation program under grant agreement N° 665207).

REFERENCES

1. I. Ihrke, J. Restrepo, and L. Mignard-Debise, IEEE Signal Process. Mag. Inst. Electr. Electron. Eng. **33**, 59 (2016).
2. A. Gershun, J. Math. Phys. **18**, 51 (1939).
3. M. Levoy and P. Hanrahan, Proc. SIGGRAPH pp. 31–42 (1996).
4. E. A. Deem, Y. Zhang, L. N. Cattafesta, T. W. Fahringer, and B. S. Thurow, Meas. Sci. Technol. **27**, 084003 (2016).
5. M. W. Tao, S. Hadap, J. Malik, and R. Ramamoorthi, 2013 IEEE Int. Conf. on Comput. Vis. pp. 673–680 (2013).
6. E. Y. Lam, J. Opt. Soc. Am. A **32**, 2021 (2015).
7. M. Levoy, R. Ng, A. Adams, M. Footer, and M. Horowitz, ACM Transactions on Graph. **25**, 924 (2006).
8. T. Georgiev and A. Lumsdaine, Eurographics 2009 pp. 5–8 (2009).
9. C. Perwaß and L. Wietzke, Proc. SPIE **8291**, 4 (2012).
10. S. Zhu, A. Lai, K. Eaton, P. Jin, and L. Gao, Appl. Opt. **57**, A1 (2018).
11. R. P. O'Shea, S. G. Blackburn, and H. Ono, Vis. research **34**, 1595 (1994).
12. M. Broxton, L. Grosenick, S. Yang, N. Cohen, A. Andalman, K. Deisseroth, and M. Levoy, Opt. Express **21**, 25418 (2013).
13. M. Turola, Ph.D. thesis, City Univ. Lond. (2016).
14. C.-K. Liang and R. Ramamoorthi, ACM Transactions on Graph. **34**, 1 (2015).
15. T. Georgiev and A. Lumsdaine, Comput. Graph. Forum **29**, 1955 (2010).
16. T. Georgiev and A. Lumsdaine, J. Electron. Imaging **19**, 021106 (2010).
17. R. Ng, Ph.D. thesis, Stanf. Univ. (2006).
18. M. Martínez-Corral and B. Javidi, Adv. Opt. Photonics **10**, 512 (2018).
19. E. Hecht, *Optics* (Pearson Education, 2017), fifth edit ed.

FULL REFERENCES

1. I. Ihrke, J. Restrepo, and L. Mignard-Debise, "Principles of Light Field Imaging: Briefly revisiting 25 years of research," IEEE Signal Process. Mag. Inst. Electr. Electron. Eng. **33**, 59–69 (2016).
2. A. Gershun, "The Light Field," J. Math. Phys. **18**, 51–151 (1939).
3. M. Levoy and P. Hanrahan, "Light Field Rendering," Proc. SIGGRAPH pp. 31–42 (1996).
4. E. A. Deem, Y. Zhang, L. N. Cattafesta, T. W. Fahringer, and B. S. Thurow, "On the resolution of plenoptic PIV," Meas. Sci. Technol. **27**, 084003 (2016).
5. M. W. Tao, S. Hadap, J. Malik, and R. Ramamoorthi, "Depth from Combining Defocus and Correspondence Using Light-Field Cameras," 2013 IEEE Int. Conf. on Comput. Vis. pp. 673–680 (2013).
6. E. Y. Lam, "Computational photography with plenoptic camera and light field capture: tutorial," J. Opt. Soc. Am. A **32**, 2021–2032 (2015).
7. M. Levoy, R. Ng, A. Adams, M. Footer, and M. Horowitz, "Light Field Microscopy," ACM Transactions on Graph. **25**, 924–934 (2006).
8. T. Georgiev and A. Lumsdaine, "Depth of Field in Plenoptic Cameras," Eurographics 2009 pp. 5–8 (2009).
9. C. Perwaß and L. Wietzke, "Single Lens 3D-Camera with Extended Depth-of-Field," Proc. SPIE **8291**, 4– (2012).
10. S. Zhu, A. Lai, K. Eaton, P. Jin, and L. Gao, "On the fundamental comparison between unfocused and focused light field cameras," Appl. Opt. **57**, A1–A11 (2018).
11. R. P. O'Shea, S. G. Blackburn, and H. Ono, "Contrast as a Depth Cue," Vis. research **34**, 1595–1604 (1994).
12. M. Broxton, L. Grosenick, S. Yang, N. Cohen, A. Andalman, K. Deisseroth, and M. Levoy, "Wave optics theory and 3-D deconvolution for the light field microscope," Opt. Express **21**, 25418 (2013).
13. M. Turola, "Investigation of plenoptic imaging systems: a wave optics approach," Ph.D. thesis, City Univ. Lond. (2016).
14. C.-K. Liang and R. Ramamoorthi, "A Light Transport Framework for Lenslet Light Field Cameras," ACM Transactions on Graph. **34**, 1–19 (2015).
15. T. Georgiev and A. Lumsdaine, "Reducing plenoptic camera artifacts," Comput. Graph. Forum **29**, 1955–1968 (2010).
16. T. Georgiev and A. Lumsdaine, "Focused plenoptic camera and rendering," J. Electron. Imaging **19**, 021106 (2010).
17. R. Ng, "Digital light field photography," Ph.D. thesis, Stanf. Univ. (2006).
18. M. Martínez-Corral and B. Javidi, "Fundamentals of 3D imaging and displays: a tutorial on integral imaging, light-field, and plenoptic systems," Adv. Opt. Photonics **10**, 512 (2018).
19. E. Hecht, *Optics* (Pearson Education, 2017), fifth edit ed.